Bullet Time Taylor-Couette: Unwrapping the 360 Degree Field of View for Rheoscopic Flow Visualization

Muller, K.; Greidanus, A.J.; Dash, A.; Poelma, C.

Publication date
2022

Document Version
Final published version

Published in
20th International Symposium on Applications of Laser and Imaging Techniques to Fluid Mechanics

Bullet Time Taylor-Couette: Unwrapping the 360 Degree Field of View for Rheoscopic Flow Visualization

K. Muller[1]*, A.J. Greidanus[1], A. Dash[1], C. Poelma[1]
1: Multiphase Systems (Process & Energy), Faculty of Mechanical, Maritime and Materials Engineering, Delft University of Technology, The Netherlands
* Correspondent author: K.Muller@tudelft.nl

Keywords: Circular Taylor-Couette Flow, Dynamic Pattern Formation, Rheoscopic Flow Visualization, Panorama Imaging, Texture Mapping, Particle-Laden Flow

ABSTRACT

The circular Taylor-Couette flow is one of the archetypical model systems for the study of flow transitions and dynamic pattern formation in experimental fluid dynamics. The emergence of the internal vortical flow structures are commonly visualized through a rheoscopic flow visualization, while their spatio-temporal dynamics can be extracted by the construction of a space-time diagram using a single camera. Although the latter is an effective method to map the various flow regimes for different inner and outer cylinder rotations, it suffers from limitations in the frame rate while the full extent of the azimuthal vortex structure along the circumference, together with its dynamic evolution through space and time, remains unclear. In this work, we perform the full 360-degree field of view panorama imaging for the rheoscopic flow visualization of the azimuthal vortex structure that wraps around the circumference. We use a set of 12 GoPro cameras that are commercially available and can be triggered remotely. We calibrate and position our cameras using methods from computer vision while we synchronize their audio channels at an inter-frame precision much greater than the frame rate. We unwrap the physical coordinates along the circumference of the outer cylinder through texture mapping its surface using a spatially weighted image interpolation and present a single representation of the azimuthal vortex structure from the rheoscopic flow visualization. We validate our methods within a submillimeter precision and showcase the application to study the steady-state and transient dynamics of a single-phase wavy vortex flow. Furthermore, we discuss the current limitations as we add neutrally buoyant PMMA particles at increasing volume fractions up to 30 %. Our methods allow us to fully decouple space and time, and study the dynamic pattern formation at bullet time accuracy.

1. Introduction

The Taylor Couette setup is a classical facility in experimental fluid dynamics to study the forced convection of a fluid that is submerged between two concentric cylinders; displaying a broad variety of flow transitions depending on the inner and outer cylinder rotation (Koschmieder, 1993; Grossmann, 2019). Most notably are the emergence of complex vortex structures that stack

between the inner and outer cylinders in the axial direction and wrap around its circumference along the azimuthal coordinate. Such vortex structures include the laminar and turbulent Taylor rolls, wavy vortex flow, and spiral vortices, to name a few. Introducing particles to the flow furthers a rich set of multiphase flow behaviors, including novel flow transitions (Majji, 2018), co-existing states and breaking of the azimuthal symmetry (Ramesh, 2019), effects of particle migration (Baroudi, 2020), and most recently provided evidence of an azimuthally localized wavy vortex flow (Dash, 2020).

To visualize the flow structures that wrap around the circumference, it is common practice to seed the fluid with a small amount of highly reflective flakes that align with the direction of the flow. Such a rheoscopic flow, or kalliroscopic fluid, visualization (Borrero-Echeverry, 2018) provides the visual dynamic pattern formation at the outer cylindrical surface and is a well-documented method to map the various flow regimes, with previous demonstrations in both single and multiphase flow. Furthermore, to extract the spatio-temporal dynamics of the complex vortex structures, it is popular to construct a space-time diagram, imaging the flow visualization over the height of the outer cylinder using a single camera. Although this is an effective method to study the dynamic evolution of the longitudinal wave number in the axial direction, it is limited by the camera frame rate due to the finite rotation speed and does not capture the full extent of the vortex structure along the circumference of the outer cylinder; obviously lacking knowledge of the azimuthal wave number which requires a full 360-degree panorama field of view, imaging all around the outer cylinder, to fully decouple space and time.

While previous efforts to image the rheoscopic flow in full 360 degrees around the outer cylinder date back to the seminal work by Gorman and Swinney (1983) using a single camera and a complex mirror arrangement, only most recently, Bourgoin and Huisman (2020) have demonstrated the application of three-dimensional particle tracking around the inner cylinder in full panorama view. Although such modern three-dimensional imaging techniques, including the application of optical tomography (Tokgoz, 2012), provide detailed insight into the internal fluid dynamics, their application is bounded in the particle density by the optical limit (Elsinga, 2006; Schanz, 2016) and, therefore, may find limited application within the scope of densely particle-laden flows. Yet, to our best knowledge, the full 360-degree field of view imaging of the rheoscopic flow visualization and fully decoupling space and time to freeze the temporal dynamics at bullet time accuracy, remains absent — ever since the original casting of The Matrix (1999).

In this work, we use a set of 12 GoPro cameras that are commercially available and can be triggered remotely. The cameras are mounted in trifocal sets around the Taylor-Couette facility and distributed to construct a full panorama view in a continuous overlap. We calibrate the cameras using methods developed in computer vision (Hartley and Zisserman, 2004) and compute their

relative positions, and viewing angles at subpixel accuracy towards the surface of the outer cylinder, supporting full knowledge of the underlying ray-tracing geometry. Furthermore, we achieve an inter-frame camera synchronization through the post hoc alignment of their audio channels (Jackson, 2016). Having synchronized the cameras and computed their positioning, we unwrap the physical coordinates through texture mapping the outer cylinder surface using a spatially weighted image interpolation. Finally, we combine the different viewing angles and construct a single representation for the azimuthal vortex structure from the rheoscopic flow visualization.

We validate our methods within a submillimeter precision using a pre-installed checkerboard wrap for calibration purposes. Subsequently, we demonstrate the application of our methods and unwrap the steady-state and transient dynamics for a single-phase flow wavy vortex. Lastly, we showcase the application to particle-laden flows as we add neutrally buoyant PMMA particles up to a 30% volume fraction and discuss the current limitations. Our methods allow us to fully decouple space and time, and study the dynamic pattern formation at bullet time accuracy.

2. Experimental Setup and 360 View Imaging System

Our Taylor Couette setup has a diameter of $22\ cm$ for the inner cylinder and $24\ cm$ for the outer cylinder, with a height of $21\ cm$ and an equal Taylor and von Karman gap of $10\ mm$. The cylinders are constructed out of $5\ mm$ thick transparent Plexiglas and secured between two stainless steel disks which are held together by 4 tension rods. Both the inner and outer cylinders are in direct drive with two individual $1.3\ kW$ three-phase motors (ABB 3GAA092520) that are mounted above and below the setup. The motors are operated through separate motor controllers (Invertek Drives) and have additional cooling fans (Wistro B20 IL-2-2) where the top motor includes a $10\ Nm$ torque sensor (AE Sensors BV). The whole system is secured in a rigid aluminum frame and provides a full 360-degree optical access around the facility, see Fig. 1.

We image around the Taylor Couette setup using a set of 12 commercially available GoPro cameras, see Fig. 1a. For the current work, we use a combination of GoPro hero black 7 and 8 cameras that are remotely triggered through a Wi-Fi connection with the GoPro Smart Remote. The cameras have an image resolution of $960 \times 1280\ px$ and $1080 \times 1920\ px$ respectively and are set to a frame rate of $240\ fps$ with an exposure time of $1/960\ sec$, well capturing the important physical detail in space and time without any motion blur. The cameras are mounted in trifocal sets and guarantee a continuous trifocal overlap between the views allowing us to cross-validate the image overlay when unwrapping the panorama view. For synchronization purposes, we record the raw audio signals at a $48\ kHz$ sampling frequency, much greater than the frame rate. Furthermore,

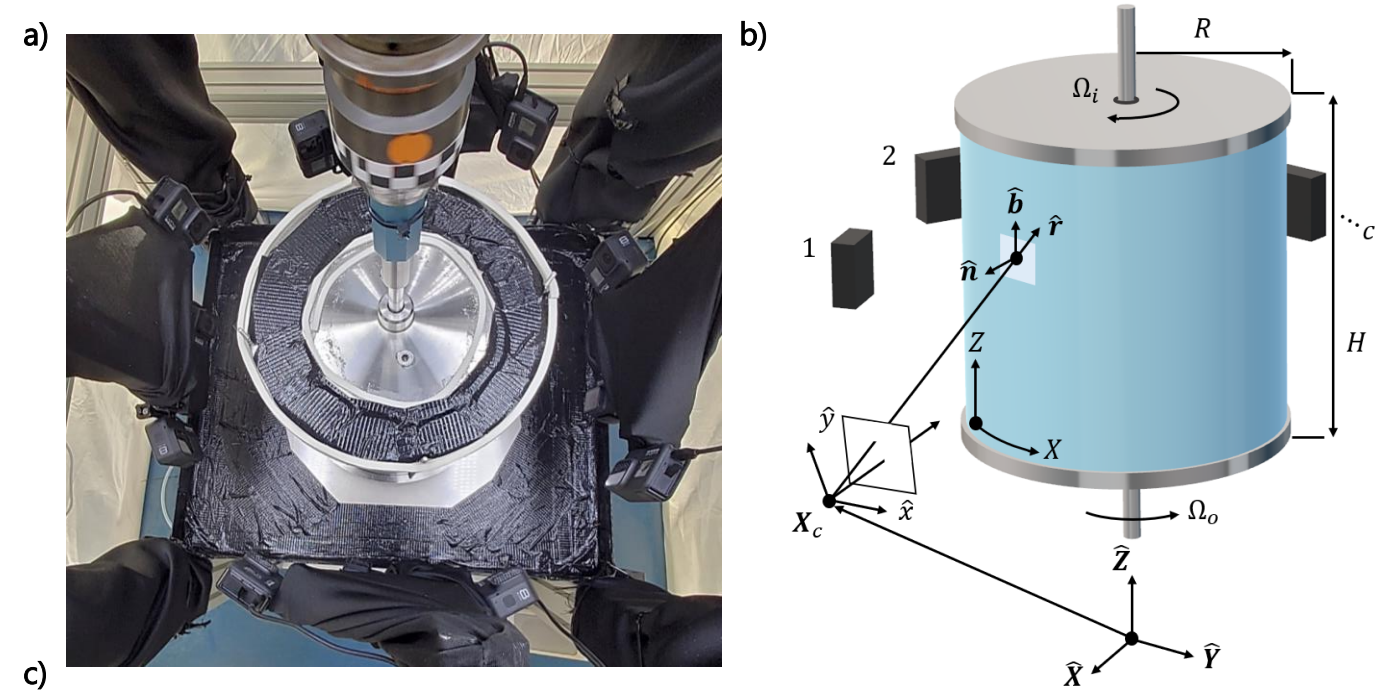

Fig. 1 Experimental setup and imaging system. a) A top view of the 12 GoPro cameras mounted around the Taylor Couette setup. b) A sketch of the Taylor Couette setup, including the global camera positioning and the ray-tracing geometry. c) The resulting camera views which are imaging in the rheoscopic fluid visualization in 360 degrees around the Taylor Couette facility.

we wrap the setup in white cloth to construct a diffuse background lighting from three 170 W LED panels (Noxion Floodlight Beam) while the inner cylinder is blackened to ensure optimal contrast with the rheoscopic seeding of $10 - 60\ \mu m$ Iriodin 100 silver pearl (Merck KGaA) at 0.1 $wt\%$.

The motors are executed through LabView using a data acquisition card (National Instruments USB 6212). For the current study, we consider only inner cylinder rotation and fix the outer motor using a mechanical rod when out of use. During operation, we sample the motor speed and torque at $1\ kHz$ and monitor the temperature every second through a USB infrared sensor (Calex PyroPen) pointed at the outer cylinder surface (emissivity 0.86). To synchronize the remotely triggered GoPro cameras and align the data acquisition we mark the start and end using a 2 and 3-second $1\ kHz$ audio cue respectively and record a 1-second cue for changes in the motor speed.

3. Camera Positioning

To unwrap the rheoscopic flow visualization along the circumference of the outer cylinder we first need an accurate correspondence between its surface and the different camera viewpoints. In this work, we use imaging techniques developed in computer vision (Hartley & Zisserman, 2004). This provides us with full knowledge of the global camera positioning and the underlying linear ray-tracing geometry towards the outer cylinder surface, see Fig. 1b, where we will neglect the minor degree of refraction through the Plexiglas wall for the current application.

First, using methods previously applied to large-scale experiments (Muller, 2020), we estimate the distortion parameters for the wide-angle GoPro fisheye lenses of Fig. 1c through rectifying lines (Devernay, 2001) and calibrate the individual cameras using the checkerboard calibration method by Zhang (2000). This provides us with the distortion correction and intrinsic calibration matrix for each view separately within a subpixel accuracy, see the top row of Tab. 1.

Secondly, we wrap the outer cylinder in a similar checkerboard print as is used for the camera calibration and position a sequence of unique marker shapes at the top and bottom rim of the outer cylinder support to globally position the cameras around the setup, see Fig. 2a. Providing a single snapshot of the wrapped outer cylinder for each view, we crop and pan the calibrated images to align the views and read out a set of nodes using image processing routines to identify edges and saddle points, see Fig. 2b. Having identified the wrap and marker positions we then find the extrinsic camera position and orientation (Hartley & Zisserman, 2004), first for each separate view in relation to the outer cylinder surface. Subsequently, we find the global viewing angle along the circumference through cross-correlation with the unique marker shapes at the top and bottom rim as we interpolate the images, see Fig. 2c.

This provides us with all the knowledge for the global camera position and orientation for all views with respect to the outer cylinder surface. The resulting camera positioning is presented in

Fig. 2d., and is further refined for the reprojection error for all views altogether. The final camera positions, the yaw-pitch-roll orientation angles, and the residual errors are reported in Tab. 1.

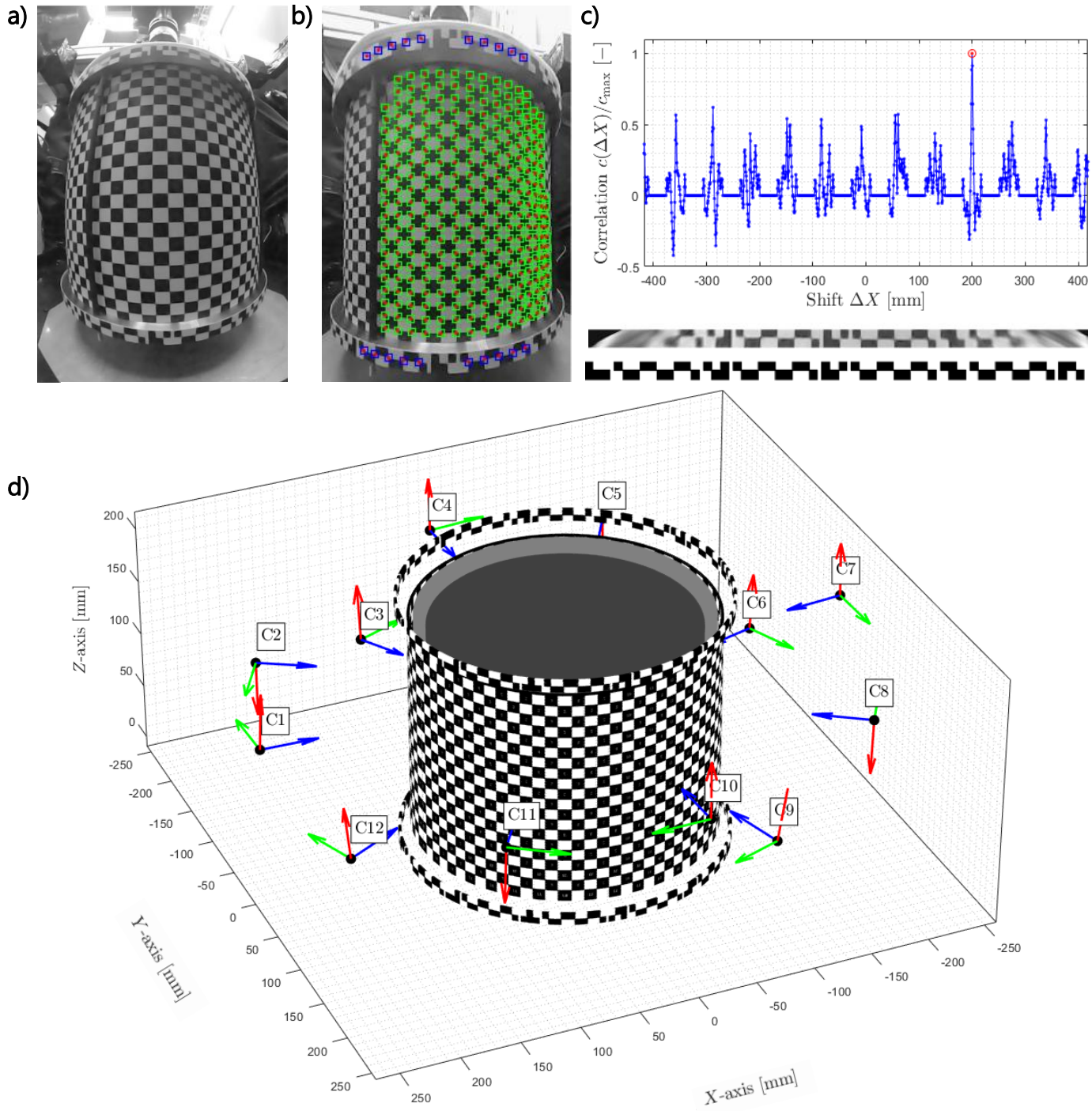

Fig. 2 Global camera positioning. a) A snapshot of the outer cylinder wrapped in checkerboard paper with a set of unique markers at the top and bottom rim. b) A panned and cropped image with identified marker position for the checkerboard wrap (green) and marker shapes at the top and bottom rim (blue). c) Position of the unique marker shape by cross-correlation with the interpolated image of the top and bottom rim. d) The resulting global camera positions for the 12 views relative to the outer cylinder.

3. Camera Synchronization

To freeze the spatio-temporal dynamics of rheoscopic flow visualization we lastly need to synchronize the remotely triggered GoPro cameras. We synchronize our cameras through their audio channels as previously applied in the field (Jackson, 2016). This supports an inter-frame synchronization at $48\ kHz$ that much greater than the frame rate of $240\ fps$ as we will neglect any delay from the speed of sound ($343\ m/s$) for an average camera spacing of $10\ cm$ that is assumed to fall well below an upper bound of a 0.07 frameshift.

First, we find the internal start of the audio acquisition τ_{acq} to remove any lag which may be present in reading the audio data of the GoPro cameras, see Fig. 3a. Secondly, we filter the audio channels for each view using a bandpass filter between 900 and $1100\ Hz$ to recover the $1\ kHz$ audio cue for the start and end of the data acquisition, see figure Fig. 3b. Performing an envelope filter over the filtered audio signals we find the start frame t_i and end frame t_e from the segmentation of the processed audio signal, see Fig. 3c and d, which we cross-validate for a consistent interval $\Delta t = t_e - t_i$ across the audio channels of the multiple cameras.

We then synchronize the cameras taking τ_{sync} as the start frame t_i for each view c, the results are appended in Tab. 1. Finally, we align the synchronized audio channels with the data acquisition, including the input from LabView and the reading of the torque, speed, and temperature sensors.

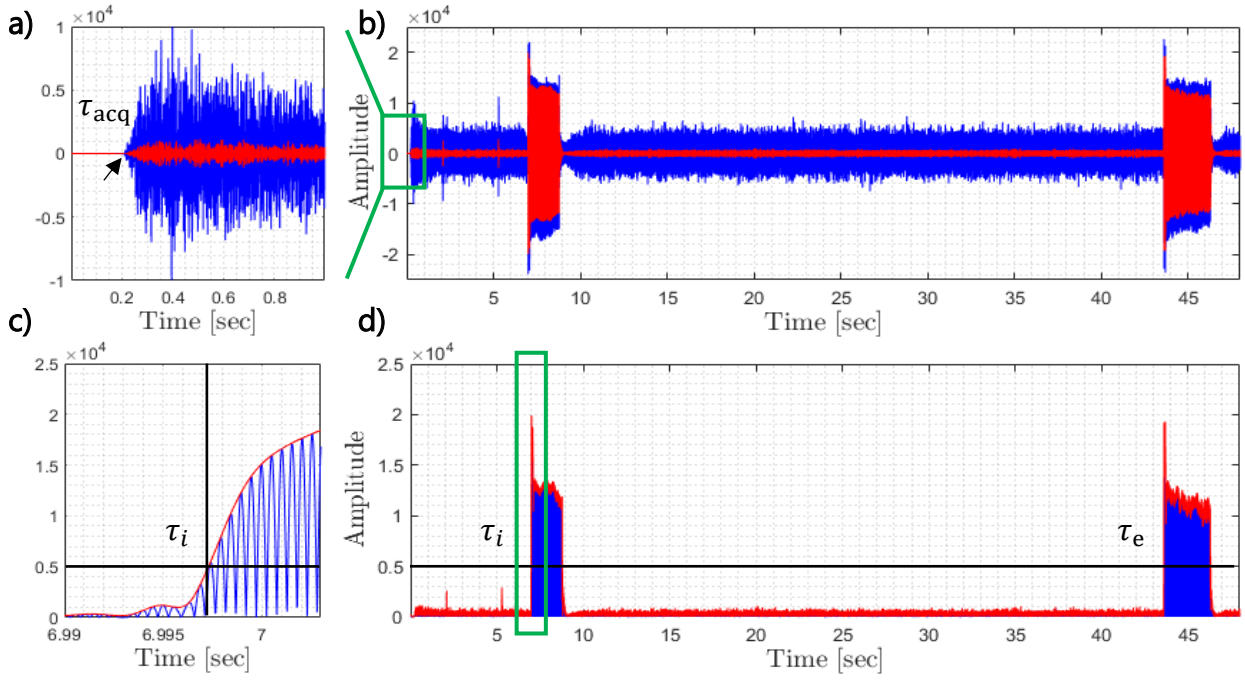

Fig. 3 Camera Synchronization. a) The internal audio lag for the GoPro cameras. b) A bandpass filtered audio signal. c) A close-up of the audio envelope segmentation. d) The envelope filtered audio signal.

Calibration	C1	C2	C3	C4	C5	C6	C7	C8	C9	C10	C11	C12
$\varepsilon_{\mathrm{cal}}$ [px]	0.32	0.33	0.23	0.36	0.31	0.24	0.28	0.31	0.29	0.35	0.30	0.21
Positioning												
X_c [mm]	265	216	93.1	12.9	-130	-211	-255	-211	-86	-9.7	142	222
Y_c [mm]	10.2	-132	-213	-254	-219	-96	-18	133	215	254	215	90.7
Z_c [mm]	141	130	78.2	144	141	80.7	144	120	86.9	150	141	76.4
α [°]	91.6	59.9	23.8	2.58	-30	-68	-87	-122	-157	-178	147	111
β [°]	-2.8	0.15	5.69	-0.3	-0.4	4.99	-1.6	1.51	6.70	-1.8	-2.0	7.01
γ [°]	-90	90.9	-92	-89	90.4	-89	-91	91.7	-86	-89	91.3	-90
$\varepsilon_{\mathrm{wrap}}$ [px]	0.53	0.39	0.30	0.59	0.33	0.30	0.40	0.25	0.43	0.48	0.29	0.29
$\varepsilon_{\mathrm{marker}}$ [px]	1.31	1.72	0.80	0.93	1.48	1.21	1.00	0.39	1.28	0.96	1.01	0.65
Synchroniza-tion												
τ_{acq} [ms]	1.71	23.2	2.63	24.2	0	1.96	22.7	2.63	6.01	4.19	2.23	1.69
τ_{sync} [s]	0.42	0.44	0.37	0.46	0.43	0.39	0.46	0.43	0.38	0.42	0.44	0

Tab. 1 Results and accuracy for the camera calibration, positioning, and synchronization. To mark the differences in the internal audio lag and synchronization we zero the audio signals for cameras 5 and 12 at reference.

5. Unwrapping The Taylor Couette

Having synchronized the cameras at an inter-frame accuracy and provided with full knowledge of the relative camera positioning in relation to the outer cylinder, we now unwrap the physical coordinate through texture mapping the outer cylindrical surface of the Taylor Couette setup. First, we construct a spatial weighting function to smoothly combine the images from multiple viewpoints. Secondly, we validate the accuracy of the image overlay from the checkerboard wrapping that was installed for calibration purposes. Finally, we apply the spatially weighted image interpolation to unwrap a wavy vortex flow and present the resulting 360-degree panorama field of view for the rheoscopic flow visualization.

At the top of Fig. 4, we first unwrap the first camera view by naïvely interpolating the raw intensity values along with the coordinates of the outer cylinder surface. Obviously, this includes the interpolated intensity values that sit at the rear arc of the cylinder and are not visible in our selected camera view. Therefore we introduce a spatial weighting function w_{ij} for each pixel location (i, j) at the outer cylinder surface in object space that we construct from the underlying ray-tracing geometry to smoothly mask the frontal arc of the cylinder for each view c, assuming uniform lighting conditions all around the setup.

We compute our weighting function w_{ij} from the reflection angle $\alpha_{ij} = \angle(-\hat{\boldsymbol{r}}_{ij}, \hat{\boldsymbol{n}}_{ij}) = \arccos(-\hat{\boldsymbol{r}}_{ij} \cdot \hat{\boldsymbol{n}}_{ij})$ between the surface normal $\hat{\boldsymbol{n}}_{ij}$ and the incident ray-director $\hat{\boldsymbol{r}}_{ij}$, see Fig. 1b. To make the weighting function w_{ij} independent over the height of the cylinder we project the ray-director $\hat{\boldsymbol{r}}_{ij}$ onto the plane spanned by the bi-normal vector $\hat{\boldsymbol{b}}$ and define the plane ray-director $\hat{\boldsymbol{r}}'_{ij} = (I - \hat{\boldsymbol{b}}\,\hat{\boldsymbol{b}}^{\mathrm{T}})\boldsymbol{r}_{ij} / \sqrt{1 - \hat{\boldsymbol{b}}^{T}\hat{\boldsymbol{r}}_{ij}{}^{2}}$, with I the identity matrix and T the vector transpose. Substituting the ray-director for the reflection angle with the plane ray-director, we then define our weighting function as the reflective area that is projected in the direction of the camera:

$$w_{ij} = \cos(a_{ij}) = -\hat{\boldsymbol{r}}'_{ij} \cdot \hat{\boldsymbol{n}}_{ij}. \qquad (1)$$

When the surface normal $\hat{\boldsymbol{n}}_{ij}$ points directly into the camera view $w_{ij} = 1$, when the surface normal is exactly aligned perpendicular $w_{ij} = 0$, and when facing away from the camera view $w_{ij} = -1$ from which we segment the frontal arc of the cylinder in view of the camera by $w_{ij} \geq 0$.

The results for the weighted image interpolation are shown in the middle of Fig. 4 for two consecutive views, clearly masking the frontal arc while smoothly transitioning the edges. Subsequently, performing a summation over all the unwrapped views and normalizing along the azimuthal direction, we present the full 360-degree field of view and find that the images nicely overlay. Lastly, we test our camera mappings at a finite outer rotation speed of $\Omega_o \sim 1\,Hz$ at the bottom of Fig. 4. Above the red line, we find a misalignment between the unwrapped image frames. Below the red line, we cancel this misalignment as we compute the image displacement between consecutive unwrapped snapshots and shift the frames at an inter-frame accuracy, and find little to no visual motion blur. This validates the accuracy of our camera mappings and audio synchronization within $0.67\,mm$ as we sample 15 pixels per $10\,mm$ tile dimension.

Finally, we unwrap the rheoscopic flow visualization for a steady-state wavy vortex at finite inner cylinder rotation $\Omega_i \sim 1\,Hz$ with a shear Reynolds number of $Re_s \sim 600$. First, we subtract a background image that is patched from multiple still images for each view separately. Secondly, we unwrap the individual views and perform a $45 \times 45\,px$ min-max image normalization as we align the images at inter-frame accuracy, see the top Fig. 5. We then perform the weighted image interpolation and sum the individual views, which we normalize along the azimuthal direction and post-process reapplying the min-max image filter. The final fully unwrapped rheoscopic flow visualization is presented at the bottom of Fig. 5. Despite minor artifacts from the 4 tension rods (see Fig. 1c), we fully recover the wavy vortex pattern that tiles the entire circumference and provides access to the simultaneous measurement of the azimuthal and longitudinal wavenumbers. This demonstrates that we can fully decouple space and time, and freeze the flow at a bullet time accuracy greater than the frame rate of the cameras.

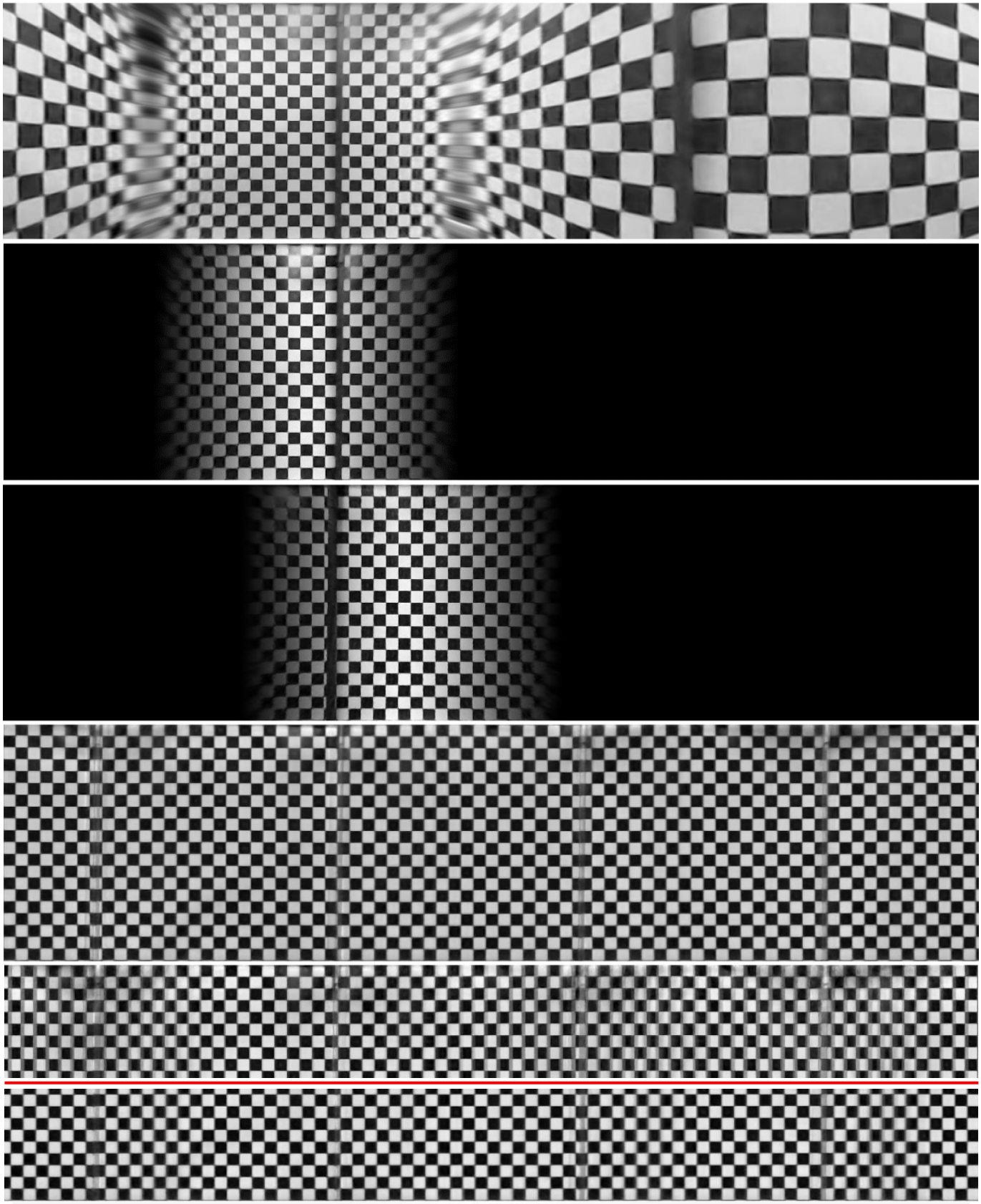

Fig. 4 Unwrapping the checkerboard wrap. From top to bottom: a naïvely interpolated image across the circumference of the outer cylinder, the spatially weighted image interpolation for two consecutive views, the combined panorama view in 360 degrees, and finally, the inter-frame aligned panorama view at finite rotation.

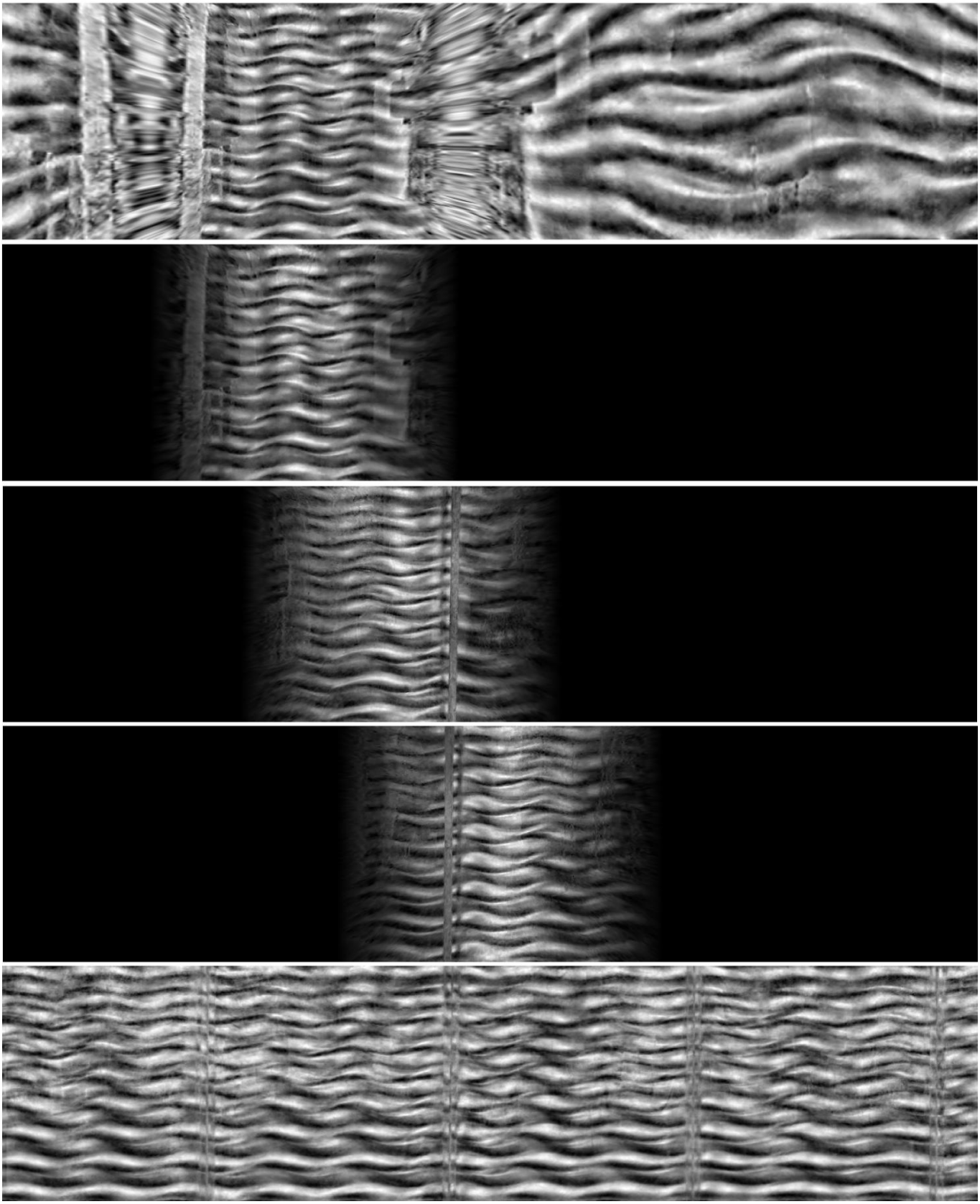

Fig. 5 Unwrapping the full 360 degrees field of view for the rheoscopic flow visualization of a wavy vortex flow. From top to bottom: the unwrapped background-subtracted image for a single view, the spatially weighted image interpolation for three consecutive views, and finally, the wavy vortex flow in a full panorama view.

7. Results and Discussion

Having validated the accuracy of our camera mappings and audio synchronization from the pre-installed calibration wrap, and successfully the overlayed the images from the different unwrapped views for the rheoscopic flow visualization of a wavy vortex flow, we now demonstrate the application of our methods to study the transient dynamics and showcase the application to multiphase flow experiments as we add neutrally buoyant PMMA particles.

In Fig. 6, we present results obtained for the transient dynamics of the wavy vortex flow of Fig. 5 that is developing at startup. Firstly, at $t \simeq 0.1\,sec$, although weakly visible within the background noise, we find a near-instantaneous emergence of a regular wave pattern, just before the flow starts to develop from the upper and lower von Karman gap. Secondly, from $t \simeq 0.3$ to $t \simeq 1\,sec$, we find the initial development of laminar Taylor rolls that rapidly propagate inward from the top and bottom of the cylinder, in a finite time. Subsequently, from $t \simeq 1\,sec$, we find the emergence of randomly distributed topological defects that break down the laminar Taylor rolls, and finally, from roughly $t \simeq 2$ to $t \simeq 5\,sec$, we find the development of sporadically modulating waves preceding the development of the steady wavy vortex flow of Fig. 5.

Lastly, in Fig. 7, we present results obtained for steady-state flow measurements with the addition of $600\,\mu m$ PMMA particles (Goodfellow $1.19\,g/cm^3$) which we add to our glycerol water mixture (Boom Glycerol 1.23) that is matched in density (Volk & Kahler, 2018). From the top to bottom, we increase the volume fraction from $\phi_F = 6$ to $30\,\%$ and suppress the effective Reynolds number as we ramp up the suspension viscosity approximately 3 fold. Firstly, we find that the image quality is gradually degrading as the rheoscopic contrast is suppressed. Despite the degrading image quality, we do get good insight into the azimuthal wave structure which shows an increasing amount of variation with an increasing volume fraction, and finally, at $\phi_F = 30\,\%$, we find that the flow regime breaks down into a partially spiraling vortex flow that lacks azimuthal symmetry.

In summary, this showcases many interesting transient and steady-state flow features that we can now directly obtain from the instantaneous flow snapshot, and may not be available when imaging the rheoscopic flow visualization using a single camera.

8. Conclusions

In this work, we have demonstrated the proof of principle to unwrap the full 360-degree field of view for the rheoscopic flow visualization inside the circular Taylor Couette using a set of 12 commercially available GoPro cameras. Firstly, using versatile camera techniques developed in computer vision we successfully positioned a set of calibrated cameras and achieved an accurate

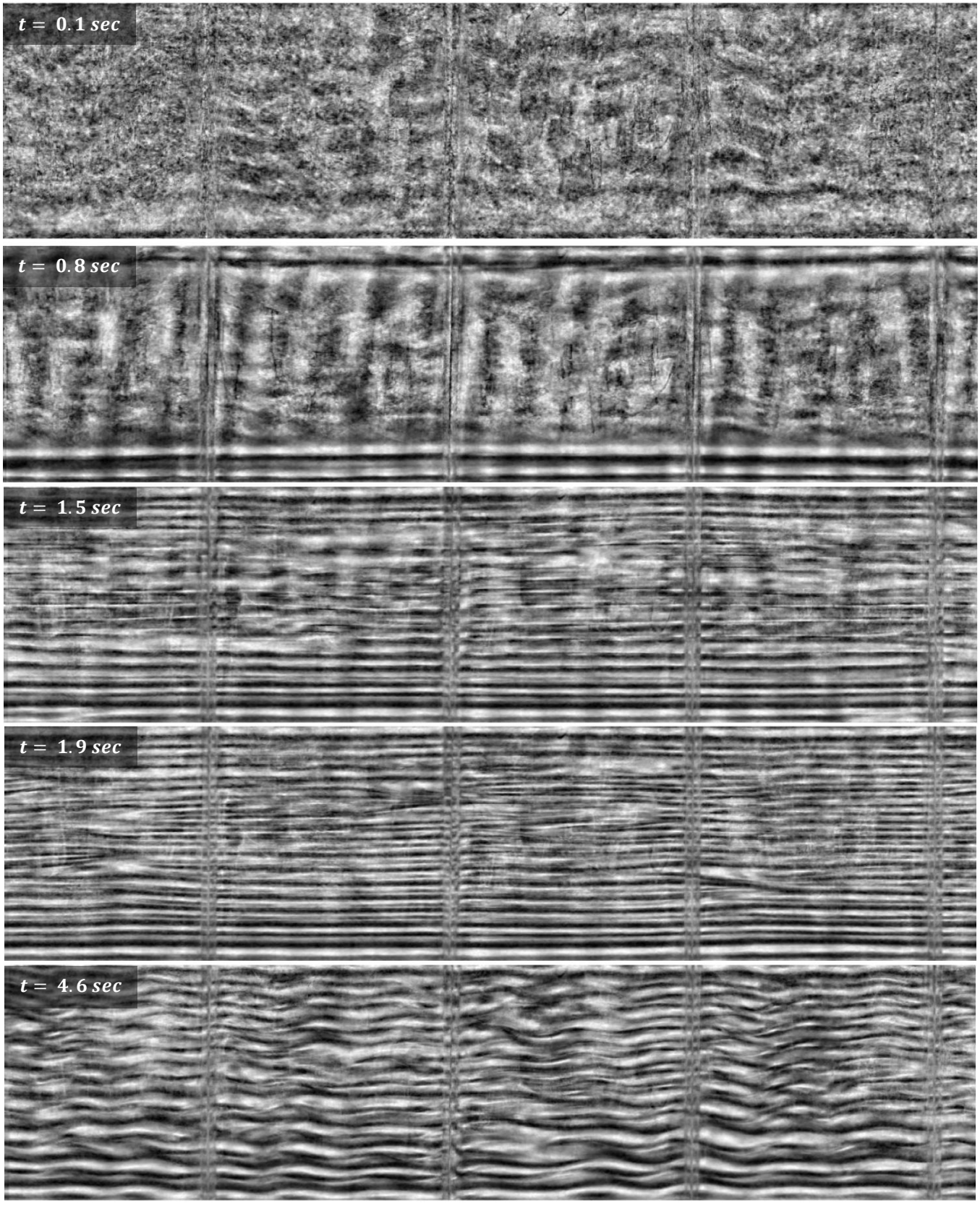

Fig. 6 Transient dynamics for the wavy vortex flow. From top to bottom showcasing the initial frame just after start-up, development of inward propagating (laminar) Taylor rolls, the emergence of topological defects, and finally randomly modulated waves preceding the wavy vortex flow.

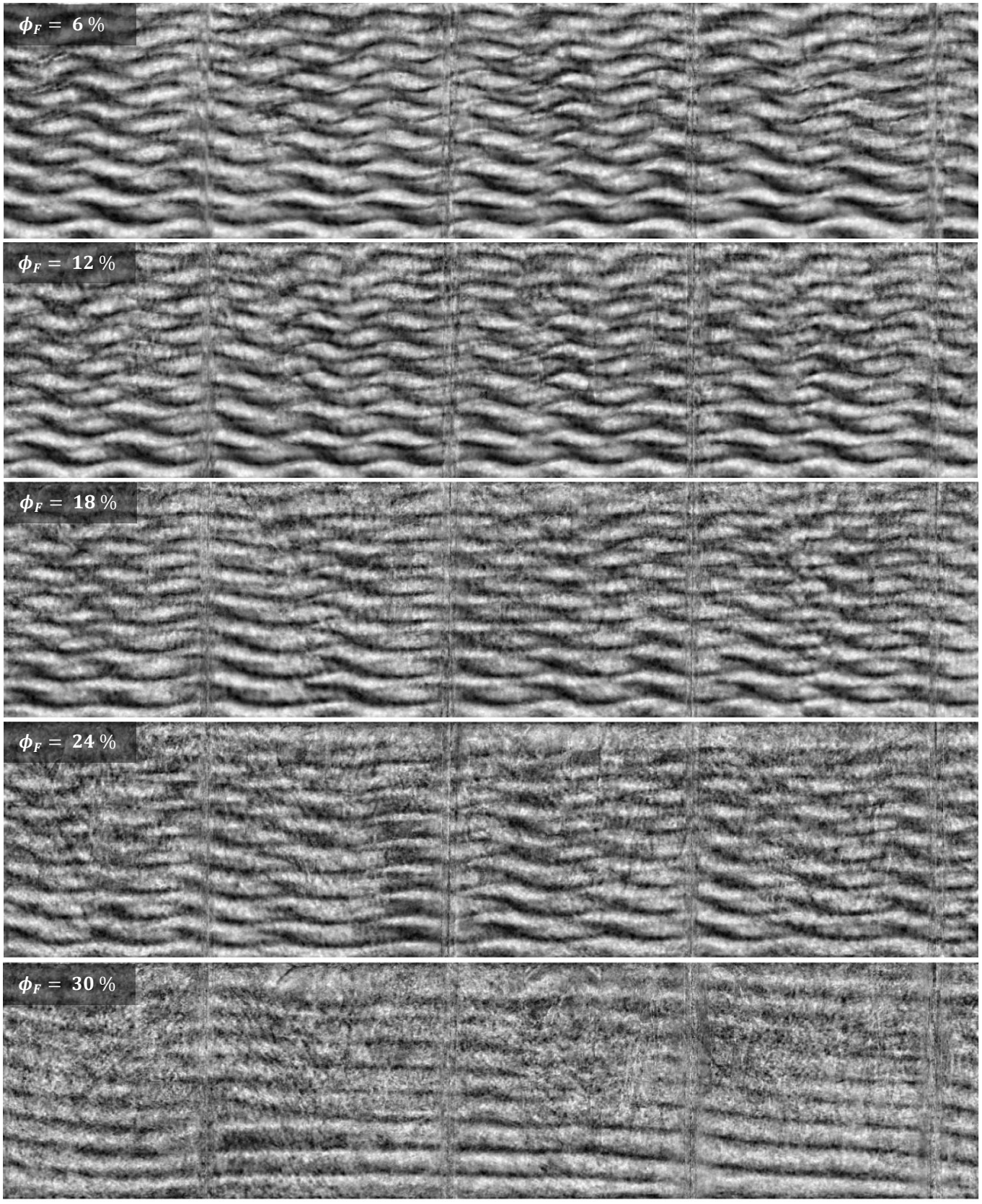

Fig. 7 Steady-state dynamics for particle-laden flow. From top to bottom: the addition of $600\ \mu m$ PMMA particles at different volume fractions for $\phi_F = 6, 12, 18, 24$ and $30\ \%$ gradually degrading the image quality and increasing the suspension viscosity.

mapping between the outer cylinder surface and the individual camera views within subpixel accuracy. Secondly, we successfully synchronized the remotely triggered cameras through their audio channels at a $48\ kHz$ inter-frame precision that is much greater than the camera frame rate of $240\ fps$, allowing us to fully decouple space and time.

Unwrapping the 12 camera views we first validated the image overlap between the consecutive trifocal views. In the current work, we obtained a precision within at least $0.67\ mm$ on our pre-installed calibration wrapping, with a negligible motion blur for the inter-frame audio synchronization. Secondly, with full knowledge of the global camera position, we reconstructed the 360-degree field of view for a wavy vortex flow using a spatially weighted image interpolation from the underlying ray-tracing geometry. Finally, we showcased a result obtained for a developing wavy flow structure, including the initial formation of Taylor rolls, topological defects, and modulated waves. Furthermore, we presented results for the imaging of particle suspensions and pushed the current application up to a volume fraction of $30\ \%$. Both these demonstrations provide exciting ground to study the transient physics of the Taylor Couette flow and the effect of particles on the developing and steady-state flow structure and physics.

Our methods are easily scalable for any number of views. Furthermore, the global camera position and full knowledge of the underlying ray-tracing geometry provide promising future applications for the use of three-dimensional imaging techniques including optical tomography and particle tracking in full panorama view. Altogether, the current work presents novel ground to study the spatio-temporal dynamic pattern formation for the circular Taylor Couette flow, freezing the flow in a full 360-degree field of view at bullet time accuracy.

Acknowledgements

The authors would like to acknowledge Jan Graafland for helping with the data acquisition, and Edwin Overmars for assisting with the experiments. This work was funded by an ERC Consolidator Grant No. 725183 “OpaqueFlows”.

References

Baroudi, L., Majji, M. V., Morris, J. F. (2020). Effect of inertial migration of particles on flow transitions of a suspension Taylor-Couette flow. *Physical Review Fluids*, 5:11.

Borrero-Echeverry, D., Crowley, C. J., & Riddick, T. P. (2018). Rheoscopic fluids in a post-Kalliroscope world. *Physics of Fluids*, 30:087103.

Bourgoin, M., & Huisman, S. (2020). Using ray-traversal for 3D particle matching in the context of particle tracking velocimetry in fluid mechanics. *Review of Scientific Instruments*, *American Institute of Physics*, 91(8), 085–105.

Dash, A., Anantharaman, A., & Poelma, C. (2020). Particle-laden Taylor–Couette Flows: Higher-order Transitions and Evidence for Azimuthally Localized Wavy Vortices. *Journal of Fluid Mechanics*, 903:20.

Devernay, F., & Faugeras, O. (2001). Straight lines have to be straight: Automatic calibration and removal of distortion from scenes of structured environments. *Machine Vision and Applications*, 13(1), 14–24.

Elsinga, G. E., Scarano, F., Wieneke, B., & Oudheusden B. W. (2006). Tomographic particle image velocimetry. *Experiments in Fluids*. 41, 933–947.

Gorman, M., & Swinney, H.L. (1983). Spatial and Temporal Characteristics of Modulated Waves in the Circular Couette System. *Journal of Fluid Mechanics*, 117, 123–142.

Grossmann, S., Lohse, D., & Sun, C. (2019). High Reynolds number Taylor-Couette turbulence. *Annual Review of Fluid Mechanics*, 48(1), 53–80.

Hartley, R. I., & Zisserman, A. (2004). *Multiple View Geometry in Computer Vision*. Cambridge University Press.

Jackson, B. E., Evangelista, D. J., Ray, D. D., & Hedrick, T. L. (2016). 3D for the people: multi-camera motion capture in the field with consumer-grade cameras and open source software. *Biology Open*, 5(9), 1334–1342.

Koschmieder, E.L. (1993). *Bernard Cells and Taylor Vortices*. Cambridge Monograph on Mechanics and Applied Mathematics, Cambridge University Press.

Majji, M. V., Banerjee, S., & Morris, J. F. (2018). Inertial flow transitions of a suspension in Taylor–Couette geometry. *Journal of Fluid Mechanics*, 835, 936–969.

Muller, K., Hemelrijk, C.K., Westerweel, J., & Tam, D.S.W. (2020). Calibration of Multiple Cameras for Large-scale Experiments using a Freely Moving Calibration Target. *Experiments in Fluids*, 61:7.

Ramesh, P., Bharadwaj, S., & Alam, M. (2019). Suspension Taylor–Couette flow: co-existence of stationary and travelling waves, and the characteristics of Taylor vortices and spirals. *Journal of Fluid Mechanics*, 870, 901–940.

Schanz, D., Gesemann, S., & Schröder, A. (2016). Shake-The-Box: Lagrangian particle tracking at high particle image densities. *Experiments in Fluids,* 57:70.

Tokgoz, S., Elsinga, G. E., Delfos, R., & Westerweel, J. (2012). Spatial resolution and dissipation rate estimation in Taylor–Couette flow for tomographic PIV. *Experiments in Fluids*, 53(3), 561–583.

Volk, A., & Kähler, C. J. (2018). Density model for aqueous glycerol solutions. *Experiments in Fluids*, 59:75.

Zhang, Z. (2000). A flexible new technique for camera calibration. *IEEE Transactions on Pattern Analysis and Machine Intelligence*, 22(11), 1330–1334.